ACS APPLIED MATERIALS & INTERFACES

www.acsami.org

Research Article

Synthesis of a New Ferroelectric Relaxor Based on a Combination of Antiferroelectric and Paraelectric Systems

Chun-Hao Ma, Yi-Kai Liao, Yunzhe Zheng, Shihao Zhuang, Si-Cheng Lu, Pao-Wen Shao, Jia-Wei Chen, Yu-Hong Lai, Pu Yu, Jia-Mian Hu,* Rong Huang,* and Ying-Hao Chu*

Cite This: *ACS Appl. Mater. Interfaces* 2022, 14, 22278−22286

Read Online

ACCESS | Metrics & More | Article Recommendations | Supporting Information

ABSTRACT: Relaxor ferroelectric-based energy storage systems are promising candidates for advanced applications as a result of their fast speed and high energy storage density. In the research field of ferroelectrics and relaxor ferroelectrics, the concept of solid solution is widely adopted to modify the overall properties and acquire superior performance. However, the combination between antiferroelectric and paraelectric materials was less studied and discussed. In this study, paraelectric barium hafnate ($BaHfO_3$) and antiferroelectric lead hafnate ($PbHfO_3$) are selected to demonstrate such a combination. A paraelectric to relaxor ferroelectric, to ferroelectric, and to antiferroelectric transition is observed by varying the composition x in the $(Ba_{1-x}Pb_x)HfO_3$ solid solution from 0 to 100%. It is noteworthy that ferroelectric phases can be realized without primal ferroelectric material. This study creates an original solid solution system with a rich spectrum of competing phases and demonstrates an approach to design relaxor ferroelectrics for energy storage applications and beyond.

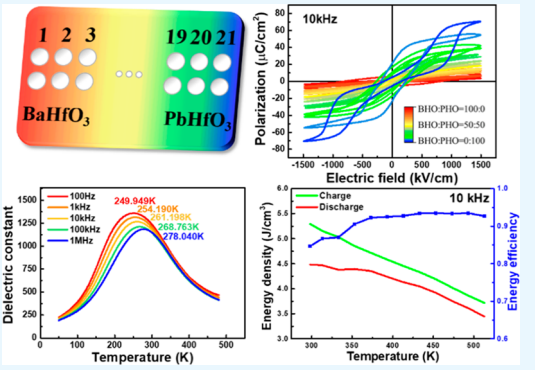

KEYWORDS: *relaxor ferroelectric, ferroelectric, energy storage, lead barium hafnate, solid solution*

Downloaded via UNIV OF WISCONSIN-MADISON on June 14, 2022 at 15:40:00 (UTC).
See https://pubs.acs.org/sharingguidelines for options on how to legitimately share published articles.

INTRODUCTION

Relaxor ferroelectric,[1−3] ferroelectric,[4] and antiferroelectric[5] behaviors are important properties of oxide ceramics and have attracted great attention because of their capabilities for various kinds of applications, including energy storages and harvests, actuators, sensors, and memories.[6−9] In this research field, the concept of solid solution is widely used to enhance the performance of original materials.[10,11] For example, $PbMg_{1/3}Nb_{2/3}O_3$ (PMN) was the first studied relaxor ferroelectric material and attracted great interest as a result of its non-trivial dielectric behavior.[12] With the combination of relaxor ferroelectric PMN and $PbTiO_3$ (PTO),[13,14] scientists created the nowadays famous relaxor ferroelectric PMN−PT solid solution with a giant piezoelectric response.[15−17] Another great example is the solid solution of ferroelectric PTO and antiferroelectric $PbZrO_3$,[18,19] which delivers the famed ferroelectric $Pb(Zr_xTi_{1-x})O_3$ (PZT) with a large polarization, fast switching rate, high Curie temperature (T_c), and high piezoelectric response.[20] Moreover, many well-known lead-free relaxor ferroelectric systems based on ferroelectric $BaTiO_3$ (BTO)[21,22] were achieved with the same concept, such as BTO−$BaSnO_3$ (paraelectric)[23] and BTO−$BaZrO_3$ (paraelectric).[24−26] However, without a ferroelectric phase, the combination between antiferroelectric and paraelectric materials was less discussed and explored. Recently, Acharya et al. demonstrated a system of $Pb_{1-x}Sr_xHfO_3$,[27] combining antiferroelectric $PbHfO_3$ and potential ferroelectric $SrHfO_3$,[28] exhibiting excellent performance for energy storage. This literature suggests the great potential of developing relaxor ferroelectrics from an antiferroelectric material-based solid solution system and, meanwhile, raises the questions: Would it possible to create relaxor ferroelectrics from a solid solution of antiferroelectric material and canonical paraelectric materials? If so, what are the possible fundamental mechanisms for inducing ferroelectricity?

A combination of antiferroelectric $PbHfO_3$ (PHO)[29,30] and paraelectric $BaHfO_3$ (BHO)[31,32] perovskites is selected as a model system as a result of their similarity of crystal structure and closely matched lattice constants (4.14 Å for PHO and 4.17 Å for BHO), which is availed to form a solid solution with an arbitrary ratio. Here, we present the realization of epitaxial $(Pb_xBa_{1-x})HfO_3$ (PBHO) films deposited on $SrTiO_3$ (STO) single-crystal substrates for further investigation. The epitaxial feature of the heterostructure can be used to simplify the model and avoid additional extrinsic influences, such as the

Received: February 8, 2022
Accepted: April 27, 2022
Published: May 6, 2022

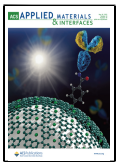

© 2022 American Chemical Society

https://doi.org/10.1021/acsami.2c02281
ACS Appl. Mater. Interfaces 2022, 14, 22278−22286

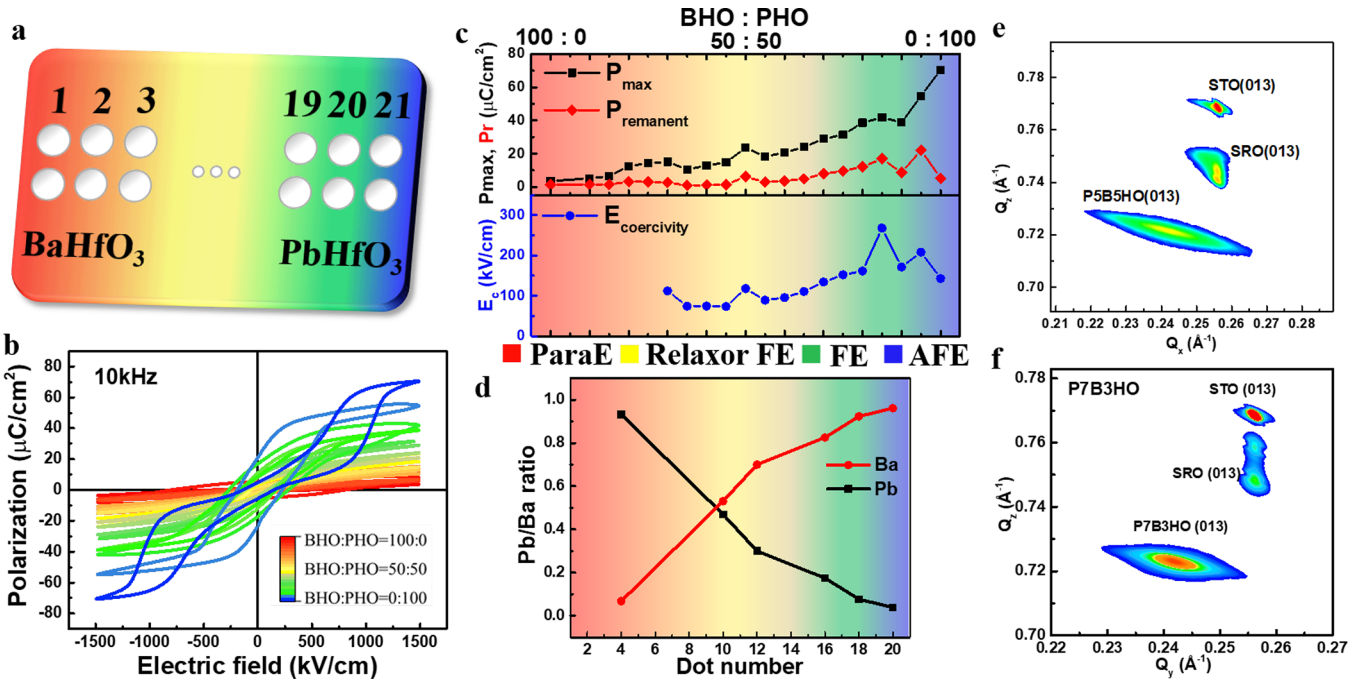

Figure 1. (a) Schematic of the compositional spread of the PBHO heterostructure. (b) *P*–*E* hysteresis loops measured at different positions marked in panel a. (c) Variation of P_{max}, P_r, and E_c corresponding to the compositions. The compositional spread is divided into four regions, including paraelectric (ParaE), relaxor ferroelectric (relaxor FE), ferroelectric (FE), and antiferroelectric (AFE) phases. (d) Pb/Ba ratio at the marked position in panel a. RSM of (e) P5B5HO and (f) P7B3HO heterostructures.

grain size, grain boundary, and orientation, which can come to play a role in determining the physical properties. To build a basic and complete understanding of PBHO solid solution, it is necessary to explore this combination by varying the composition. Moreover, it is crucial to determine the critical PHO/BHO ratio for a detailed investigation. In this study, a compositional spread of the epitaxial film from 100% BHO to 100% PHO is attempted. Through this achievement, the properties of the PBHO heterostructure with various compositions are characterized in sequence. Furthermore, relaxor ferroelectric $Pb_{0.5}Ba_{0.5}HfO_3$ is realized, even though the primal materials do not exhibit relaxor ferroelectrics. This work paves a new path for the research of relaxor ferroelectrics and introduces a new material system for prospective studies and developments.

RESULTS AND DISCUSSION

In this study, PBHO epitaxial thin films were grown on STO (001) substrates, with a $SrRuO_3$ (SRO) bottom electrode by pulsed laser deposition.[33] To investigate the composition-dependent properties of a PBHO system, a compositional spread of the PBHO film was fabricated with one side as 100% BHO and the other side as 100% PHO, as shown in Figure 1a. The ferroelectric performances of PBHO with different compositions were investigated by ferroelectric hysteresis measurements at each position marked in Figure 1a. The polarization–electric field (*P*–*E*) hysteresis loops were measured at 10 kHz, as shown in Figure 1b. A typical paraelectric *P*–*E* loop is observed with 100% BHO (red), and a characteristic antiferroelectric behavior with the double hysteresis loop is detected with 100% PHO (blue). Figure 1c shows the change of the maximum polarization (P_{max}), remnant polarization (P_r), and coercive field (E_c) from the BHO side to the PHO side. P_{max} increases from the BHO side to the PHO side, showing the ferroelectric feature of the PBHO compositional spread. Moreover, the value of P_r increases with the content of PHO, which is similar to the change of P_{max}. However, a notable drop of P_r is observed at the region close to PHO, indicating the transition from the ferroelectric phase to the antiferroelectric phase. On the basis of the ferroelectric behaviors, the composition range can be divided into four regions with the transition from paraelectric, relaxor ferroelectric, ferroelectric, and antiferroelectric phases. The composition of the compositional spread sample was determined by X-ray photoelectron spectroscopy (XPS). We measured the XPS signal of Pb and Ba, as shown in Figure S1 of the Supporting Information, point by point. With the calibration of the instrument, a ratio of Ba and Pb can be obtained, as shown in Figure 1d. With the linear fit of the data points, we can estimate the corresponding composition at the *P*–*E* loop positions. On the basis of the *P*–*E* loops, the phase boundary between paraelectric and relaxor ferroelectric is ~0.4, the phase boundary between relaxor ferroelectric and ferroelectric is ~0.6, and the phase boundary between ferroelectric and antiferroelectric is ~0.9. The smallest E_c is obtained with a value of 73 kV cm^{-1} around 45% BHO/55% PHO, and this composition is assigned as a relaxor ferroelectric phase. Meanwhile, a typical ferroelectric performance with a relative small E_c is obtained around 30% BHO/70% PHO located in the region of the ferroelectric phase, with P_{max} of 29 μC cm^{-2}, P_r of 7.9 μC cm^{-2}, and E_c of 141 kV cm^{-1}, which is confirmed as $Pb_{0.7}Ba_{0.3}HfO_3$ (P7B3HO) by XPS in Figure 1d. Here, we select these two compositions from two different phase regions as model systems for following detailed characterizations.

The structural analysis and phase identification of the PBHO/SRO/STO heterostructure were carried out by X-ray diffraction (XRD) and reciprocal space mapping (RSM) measurements. The out-of-plane θ–2θ scans of P5B5HO

https://doi.org/10.1021/acsami.2c02281
ACS Appl. Mater. Interfaces 2022, 14, 22278–22286

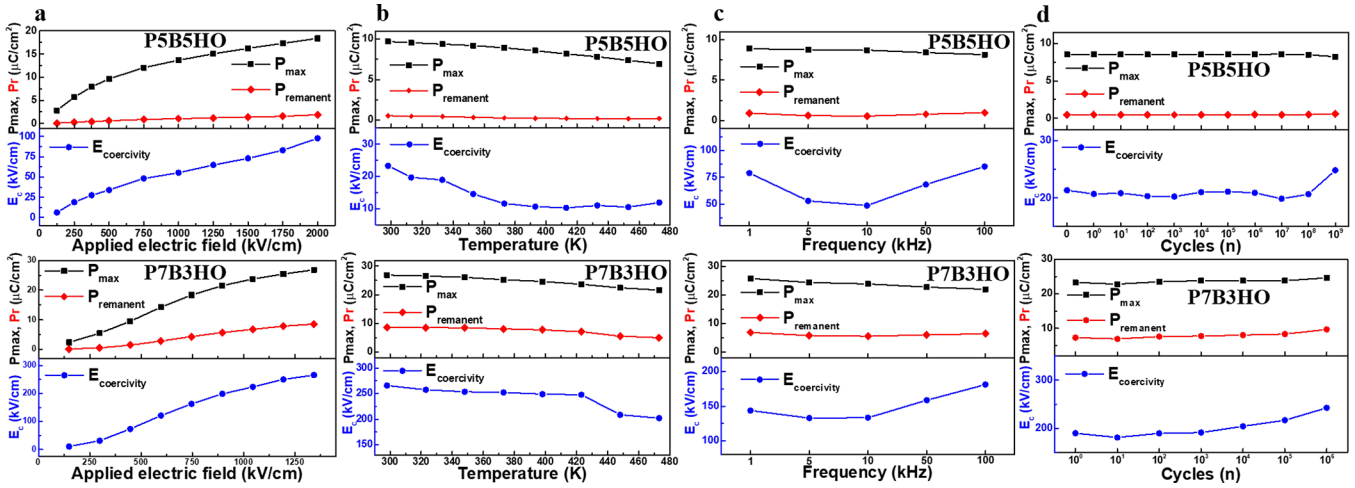

Figure 2. (a) Variation of P_{max}, P_r, and E_c of P5B5HO and P7B3HO under different electric fields. (b) P_{max}, P_r, and E_c variation corresponding to various temperatures. (c) P_{max}, P_r, and E_c variation as a function of frequency. (d) Variation of P_{max}, P_r, and E_c of P5B5HO and P7B3HO during fatigue tests.

and P7B3HO heterostructures are shown in Figure S2a of the Supporting Information. The observation of PBHO (00*l*), SRO (00*l*), and STO (00*l*) without other peaks indicates the epitaxial feature of both heterostructures. More importantly, the existence of a single PBHO (00*l*) group suggests the formation of PHO−BHO solid solution. The rocking curves of PBHO (00*l*) were measured and exhibit the full width at half maximum of 0.07° and 0.11° for P5B5HO and P7B3HO, respectively, indicating the excellent crystallinity of both heteroepitaxies, as shown in Figure S2b of the Supporting Information. In Figure S2c of the Supporting Information, the Φ scans of PBHO {202}, SRO {202}, and STO {202} in both systems are well-aligned, delivering the epitaxial relationship along the in-plane directions. Furthermore, RSM measurement was used to reveal the detailed structural information on the heteroepitaxies. As shown in Figure 1e, in the P5B5HO/SRO/STO heterostructure, the RSM around STO (013) shows that the P5B5HO film in the heteroepitaxy is almost strain-released. The lattice constants of $(P5B5HO)_{pseudocubic}$ determined from RSM are 4.16 and 4.12 Å along [001] and [010], respectively, indicating the slightly tensile and compressive strains along out-of-plane and in-plane directions. A similar result is obtained with the P7B3HO heterostructure, as shown in Figure 1f. The measured lattice constants of $(P7B3HO)_{pseudocubic}$ are 4.15 Å (001) and 4.13 Å (010), representing the small tensile and compressive strains along *c* and *b* axes. A slight structure difference was found, suggesting that the modification of the crystal structure with introducing BHO is not significant. Such a slight difference is attributed to the closely matched lattice constants of PHO and BHO. On the basis of these results, the epitaxial characteristics are confirmed with both P5B5HO and P7B3HO heterostructures, and the epitaxial relationship is determined to be $(001)_{PBHO}//(001)_{SRO}//(001)_{STO}$ and $(010)_{PBHO}//(010)_{SRO}//(010)_{STO}$.

With the confirmation of the epitaxial nature of PBHO/SRO/STO heterostructures, now we focus on the ferroelectric performance of P5B5HO and P7B3HO. Here, the macroscopic ferroelectric behaviors of these two heterostructures were studied. Figure 2a shows the *P*−*E* hysteresis loops of P5B5HO and P7B3HO heterostructures under various applied electric fields at the same frequency of 10 kHz. In addition, Figure 2a shows the change in P_{max}, P_r, and E_c values as a function of the applied electric field. The P5B5HO heterostructure exhibits classic relaxor ferroelectric *P*−*E* hysteresis loops and is stable against a large electric field (4000 kV cm^{-1}). Meanwhile, the P7B3HO heterostructure shows ferroelectricity with P_{max} of 26.9 μC cm^{-2}, P_r of 8.5 μC cm^{-2}, and E_c of 267.4 kV cm^{-1}, under an electric field of 1343 kV cm^{-1}. To further build the basic knowledge of the abilities of relaxor ferroelectric P5B5HO and ferroelectric P7B3HO, the thermal-dependent properties and electrical cyclability of these heteroepitaxies were evaluated. Figure 2b and Figure S2b of the Supporting Information display the evolution of *P*−*E* hysteresis loops and the corresponding variation of P_{max}, P_r, and E_c of P5B5HO and P7B3HO measured from room temperature to 473 K. With the increase of the temperature, it is obvious that P_{max} of P5B5HO continuously decreases and the shape of the hysteresis loop becomes more linear, indicating that the relaxor ferroelectric P5B5HO heterostructure transforms into a paraelectric state at ∼473 K. In contrast, the P7B3HO heterostructure maintains its ferroelectricity, with a ∼20% decrease of both P_{max} and P_r from room temperature to 473 K. These results suggest that P7B3HO has a higher T_c compared to P5B5HO. Besides, because the behaviors of relaxor ferroelectrics are generally frequency-sensitive, the frequency dependence of PBHO heterostructures was also inspected. As shown in Figure 2c and Figure S3c of the Supporting Information, P_{max} values of both P5B5HO and P7B3HO heterostructures are both slightly decreased with the increase of frequency. Moreover, the ferroelectric fatigue of both heterostructures was checked for multiple operation, as shown in Figure S3d of the Supporting Information. Figure 2d reveal that the P5B5HO heterostructure exhibits almost no polarization fatigue after 10^9 switching cycles; however, the P7B3HO heterostructure only maintains about 10^6 cycles. Here, these two PBHO heteroepitaxies show evidently different ferroelectric properties, indicating the strong influence made by the change of composition. Therefore, in the following sections, the relaxor ferroelectric P5B5HO and ferroelectric P7B3HO will be discussed separately.

With the initial realization of the relaxor ferroelectric P5B5HO heterostructure, it is crucial to investigate the properties of this system. To explore the thermal-induced phase transition of the P5B5HO heterostructure, Figure 3a

https://doi.org/10.1021/acsami.2c02281
ACS Appl. Mater. Interfaces 2022, 14, 22278−22286

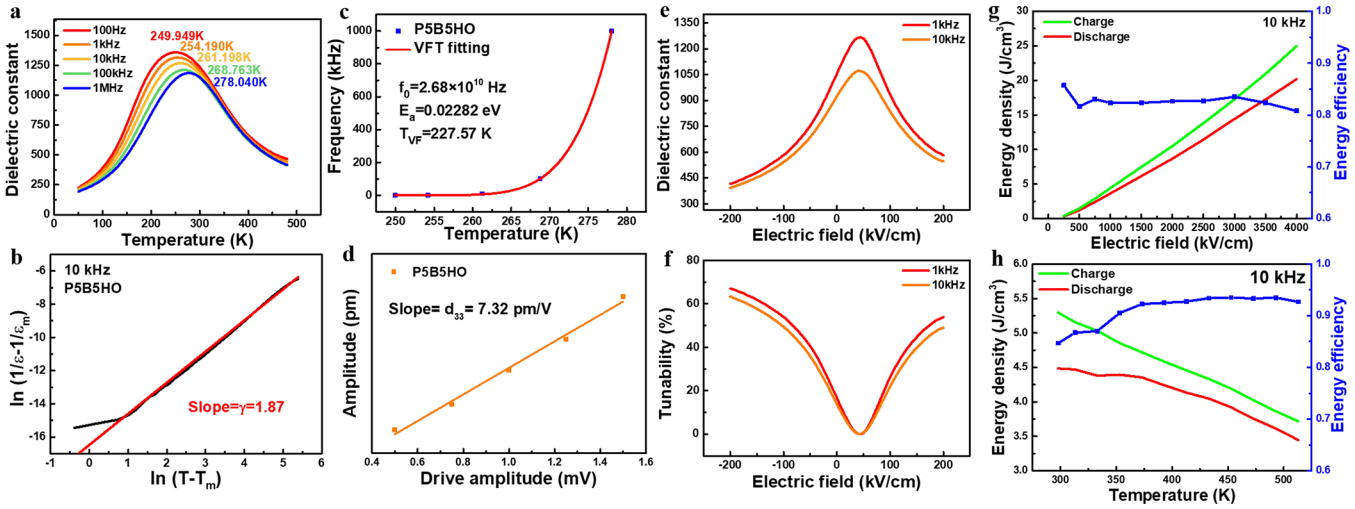

Figure 3. (a) Temperature-dependent dielectric constants of P5B5HO under various frequencies. (b) $\ln(1/\varepsilon - 1/\varepsilon_m)$ as a function of $\ln(T - T_m)$ at 10 kHz for P5B5HO. (c) Frequencies as a function of the temperature of the dielectric maximum for P5B5HO. (d) Response amplitude-drive amplitude of P5B5HO in the PFM measurement. (e) Dielectric constants of P5B5HO as a function of the electric field measured at 1 and 10 kHz. (f) Electrical tunability as a function of the electric field measured at 1 and 10 kHz. (g) U_c, U_{dis}, and η of P5B5HO measured at different electric fields. (h) U_c, U_{dis}, and η of P5B5HO measured at various temperatures.

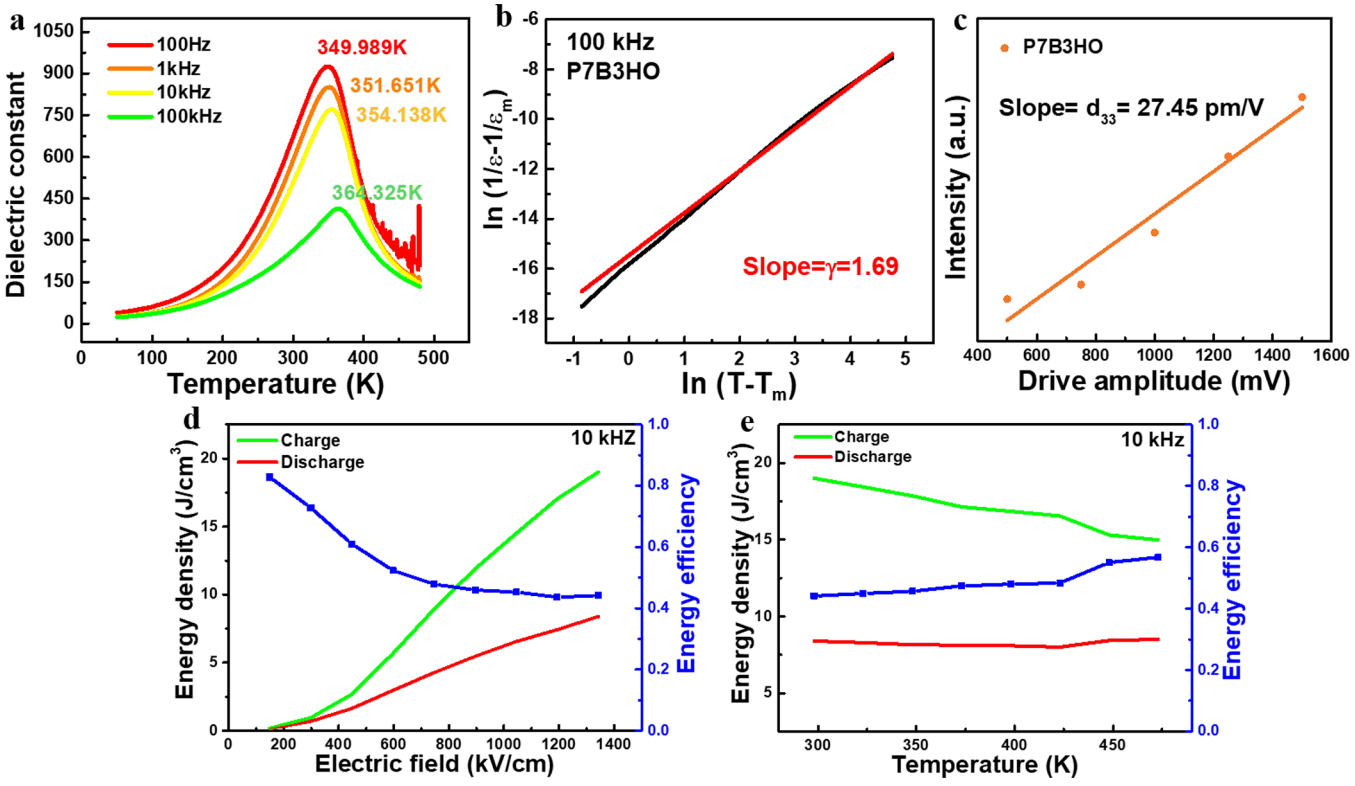

Figure 4. (a) Temperature-dependent dielectric constants of P7B3HO under various frequencies. (b) $\ln(1/\varepsilon - 1/\varepsilon_m)$ as a function of $\ln(T - T_m)$ at 10 kHz for P7B3HO. (c) Amplitude-drive amplitude of P7B3HO in the PFM measurement. U_c, U_{dis}, and η of P7B3HO measured at (d) different electric fields and (e) various temperatures.

shows the dielectric constant of P5B5HO as a function of the temperature from 50 to 480 K measured from 100 Hz to 1 MHz. The correlation between the temperature at the highest dielectric permittivity (T_m) and frequency and the broad dielectric constant peaks are corresponding to the unique diffuse phase transition in relaxor ferroelectrics. Moreover, the modified Curie−Weiss law is adopted to describe the degree of relaxor behavior. As shown in Figure 3b, P5B5HO exhibits a diffusion coefficient (γ) of 1.87 (1 for normal ferroelectric and 2 for ideal relaxor ferroelectric) at 100 kHz, which is close to the ideal value. Besides, the results from Figure 3a also exhibit a good agreement with the Vogel−Fulcher law, which is used to characterize the relationship between frequency and T_m in relaxor ferroelectrics, as shown in Figure 3c. Here, the P5B5HO heterostructure shows an activation energy of 0.023 eV, a pre-exponential factor of 2.68×10^{10} Hz, and a

https://doi.org/10.1021/acsami.2c02281
ACS Appl. Mater. Interfaces 2022, 14, 22278−22286

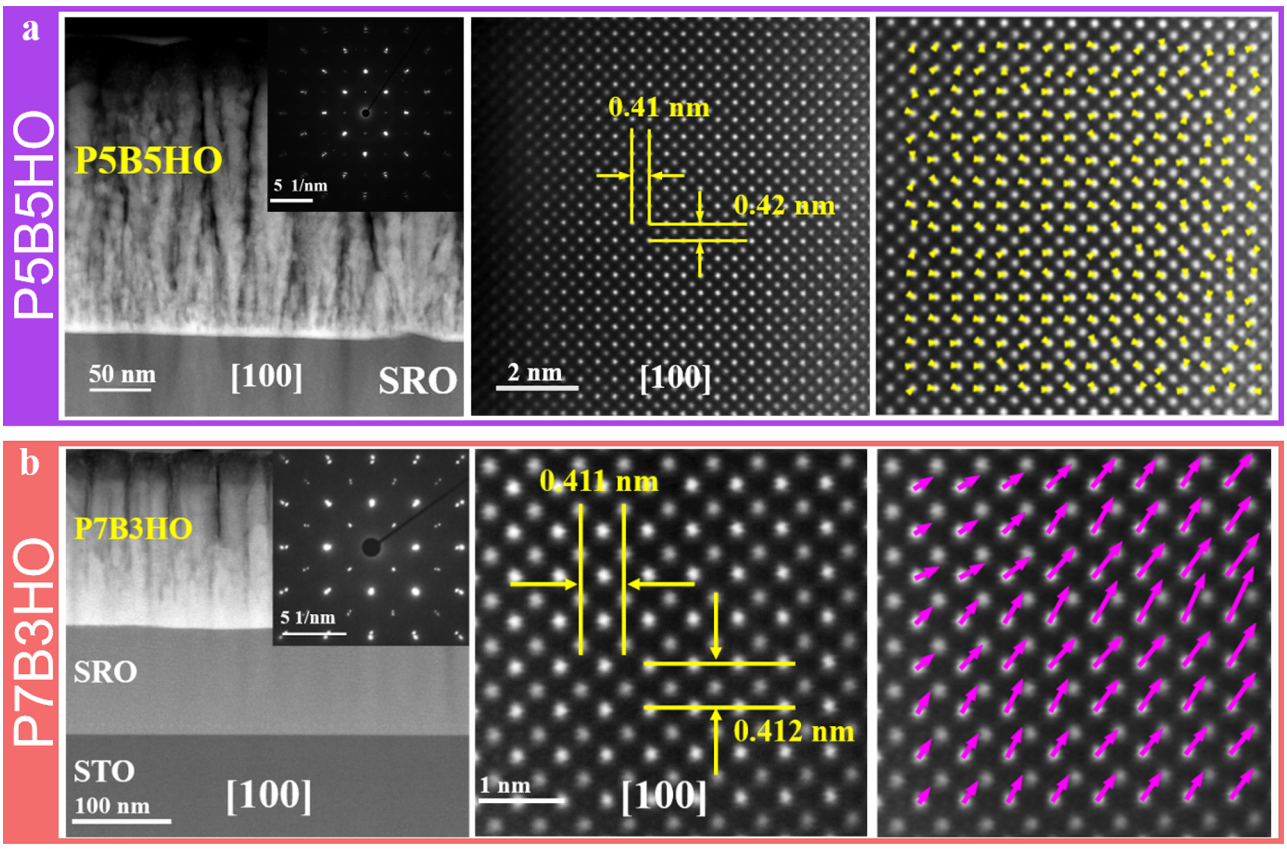

Figure 5. Low-magnification HADDF images with insets of the corresponding SADPs, atomic-resolved HAADF images, and projected displacement maps of (a) P5B5HO and (b) P7B3HO heterostructures.

freezing temperature of 227 K. In addition, the piezoelectric constant (d_{33}) of relaxor ferroelectric P5B5HO is measured by piezoresponse force microscopy (PFM), and the determined d_{33} value of the heterostructure is about 7.3 pm V^{-1}, as shown in Figure 3d. Figure 3e shows the dielectric constant under different applied electric fields. When measured at 1 kHz, the dielectric constant is evaluated from 417 to 1267 under the applied electric field between −200 and 200 kV cm^{-1}. Furthermore, the electrical tunability of the P5B5HO heterostructure is ∼67%, as shown in Figure 3f. Because relaxor ferroelectrics are treated as good candidates for energy storage, here, we convert the charge energy density (U_c), the discharge energy density (U_{dis}), and the efficiency of storage (η) from the $P-E$ measurements. Figure 3g exhibits that U_{dis} is increased with the applied electric field and η is kept over 80%. The P5B5HO heterostructure reaches the highest U_{dis} of 20.2 J cm^{-3} with η of 81% at an electric field of 4000 kV cm^{-1}. Moreover, the energy storage ability of P5B5HO in a wide range of temperatures is shown in Figure 3h. With the rise of the temperature, U_{dis} has decreased. Fortunately, as a result of the larger drop of U_c, the best η of 93.5% is achieved at 513 K. On the basis of these results, the P5B5HO heterostructure exhibits typical relaxor ferroelectric behavior, excellent dielectric tunability, and superior energy storage properties.

In addition to the P5B5HO system, the ferroelectric P7B3HO heterostructure was also investigated. Figure 4a shows the dielectric constant−temperature curves of the P7B3HO heterostructure measured from 50 to 480 K with frequencies ranging from 100 Hz to 1 MHz. Even the $P-E$ measurements display the ferroelectricity of P7B3HO, and the behavior of frequency-dependent T_m still indicates the relaxor ferroelectric feature of the heterostructure. To further determine the degree of relaxor behavior, the result from the dielectric constant−temperature curve at 100 kHz was also applied to the modified Curie−Weiss law. According to Figure 4b, the P7B3HO heterostructure shows γ of 1.69, which suggests that the P7B3HO system exhibits less degree of relaxor behavior than the P5B5HO heterostructure. Besides, the piezoelectricity of P7B3HO was investigated by PFM measurement. The characteristic butterfly loops are shown in Figure S4 of the Supporting Information. To determine the d_{33} value, the deflection of the cantilever under different voltages was measured. We used $BiFeO_3$ as a standard sample to calibrate the system right before the characterization of the PBHO system. The measured slope is used to compare to the slope of $BiFeO_3$, and then a d_{33} value can be estimated. The measurements have been repeated many times to minimize the possible artifacts of PFM, which typically gives a large variation of results. The d_{33} value of P7B3HO is determined as 27.5 pm V^{-1}, as shown in Figure 4c. In addition, the energy storage ability of P7B3HO was also checked. The external electric field-dependent U_c, U_{dis}, and η of the P7B3HO heterostructure are displayed in Figure 4d. η of this ferroelectric system is dropped from 83 to 44%, with the increase of applied bias. Figure 4e reveals the energy storage ability under a high temperature, suggesting the good thermal stability of the P7B3HO heterostructure. However, the P5B5HO heterostructure still exhibited better performance of energy storage. Here, we explored the characteristics of the P7B3HO heterostructure. In comparison to P5B5HO, P7B3HO exhibits more similarity to a normal ferroelectric material. Moreover, these results emphasize that the control of the proportion of

https://doi.org/10.1021/acsami.2c02281
ACS Appl. Mater. Interfaces 2022, 14, 22278−22286

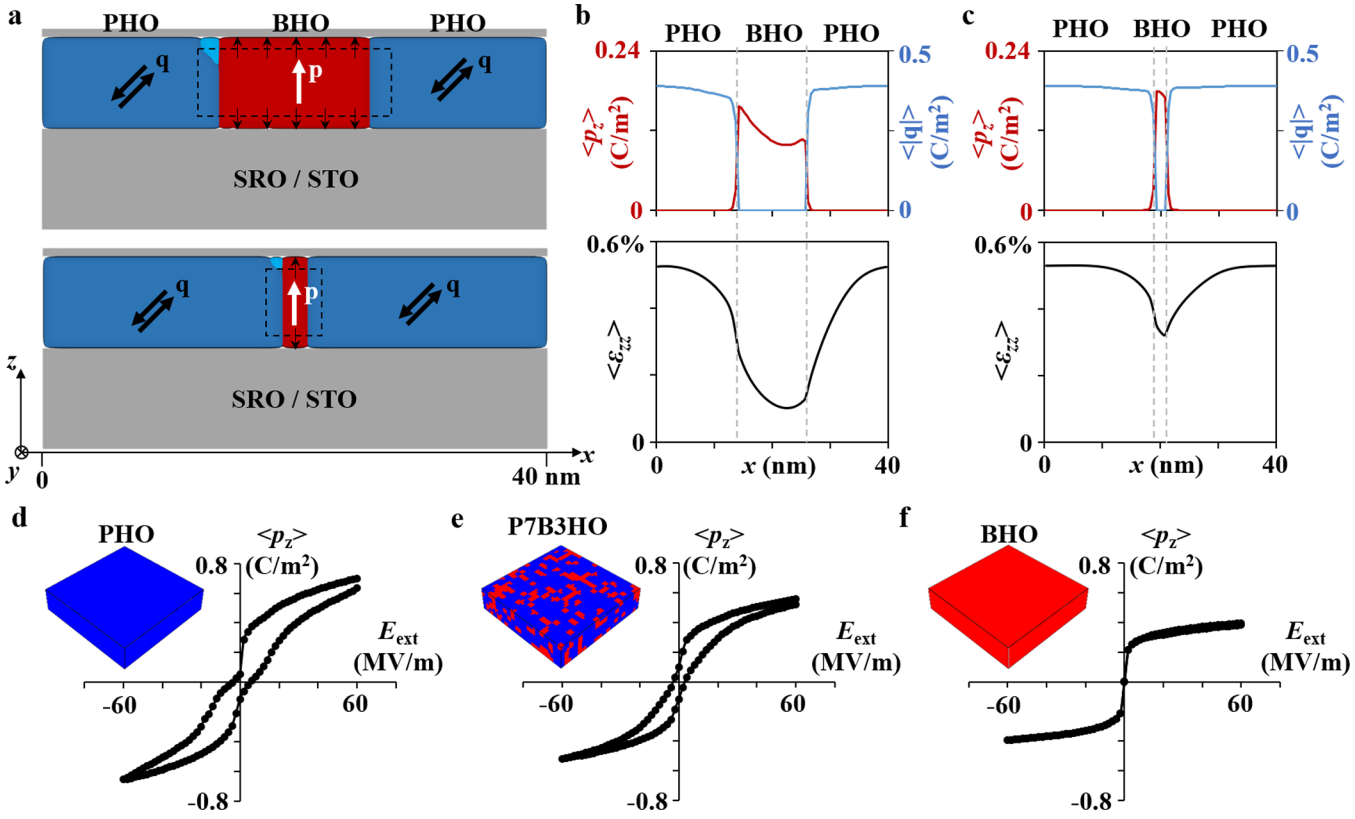

Figure 6. (a) Schematic of the PBHO heterostructure with the lateral size of BHO regions being (top) 12 nm and (bottom) 2 nm. Normalized average $\langle P_z \rangle$, $\langle |\mathbf{q}| \rangle$, and $\langle \varepsilon_{zz} \rangle$ in PBHO along the x axis with the lateral size of BHO being (b) 12 nm and (c) 2 nm. P_z, $|\mathbf{q}|$, and ε_{zz} are averaged along the z axis in the PBHO film. Simulated $P-E$ hysteresis loops of (d) pure PHO, (e) P7B3HO, and (f) pure BHO.

PHO to BHO can cause significant effects on the overall behavior of the PBHO heteroepitaxy.

After the study of macroscopic properties of the PBHO heterostructures, to further characterize the detailed microstructure and the corresponding local polarization,[34,35] high-resolution transmission electron microscopy (HRTEM) and scanning transmission electron microscopy (STEM) were carried out. To ensure the accuracy, the transmission electron microscopy (TEM) samples were prepared along two orthogonal in-plane axes, as shown in Figure S5a of the Supporting Information. Figure S5b of the Supporting Information shows the cross-sectional HRTEM images of P5B5HO taken along A and B directions, displaying the SRO/STO and P5B5HO/SRO interfaces. Moreover, the epitaxial relationship of the heterostructure obtained from TEM is consistent with the previous XRD results. Furthermore, the correlated element distribution images of major elements of P5B5HO and P7B3HO heterostructures were obtained by energy-dispersive X-ray spectroscopy (EDS) and are shown in Figure S6 of the Supporting Information. In addition, because the local polarization is correlated to the displacement of atoms inside the crystal lattices, the projected positions of each element were carefully measured by cross-sectional STEM. Figure 5a displays the low-magnification high-angle annular dark-field (HAADF) image with the inset of selected area electron diffraction patterns (SADPs), atomic-resolved HAADF image, and projected displacement map of P5B5HO. The random arrangement of local polarization is observed along both directions in the P5B5HO heterostructure, which consists of the feature of relaxor ferroelectrics. Besides, the crystal lattices and projected displacement maps along the orthogonal axes reveal the pseudocubic crystal structure of the relaxor ferroelectric P5B5HO film. In comparison, the corresponding low-magnification HAADF image, atomic-resolved HAADF image, and projected displacement map of P7B3HO are shown in Figure 5b. Here, the observation of localized oriented spontaneous polarization indicates the ferroelectric features of the P7B3HO system. According to these results, the microstructure and corresponding local polarization of P5B5HO and P7B3HO are investigated and provide clear evidence for the difference between these two heterostructures.

Phase field simulations (see the Methods) were performed to understand and model the emergence of ferroelectricity in the thin-film solid solution of antiferroelectric PHO and paraelectric BHO. As elaborated below, the simulations suggest that a non-zero spontaneous polarization can be induced in the otherwise paraelectric BHO phase through the transfer of strain from the adjacent antiferroelectric PHO across the vertical BHO−PHO interface. This is analogous to the recent observation of vertical-strain-induced ferroelectricity in the paraelectric STO phase of the STO−MgO vertical nanocomposites[36] but occurs at a much smaller spatial scale (unit cell level). In our model, the PBHO solid solution thin film is described as a mixture of PHO and BHO regions, a strategy that has been used in almost all existing phase field models for solid solution ferroelectrics,[37−41] including relaxors.[39−41] To illustrate the mechanism of interfacial-strain-induced ferroelectricity, let us first consider a simplified quasi-one-dimensional (1D) phase distribution with a 12 or 2 nm wide BHO pillar embedded in the PHO matrix. As shown in the top and bottom panels of Figure 6a, the antiferroelectric PHO regions

https://doi.org/10.1021/acsami.2c02281
ACS Appl. Mater. Interfaces 2022, 14, 22278−22286

show a single orthorhombic domain at equilibrium under zero applied electric field, consisting of pairs of antiparallel spontaneous polarizations along $[101]/[\bar{1}0\bar{1}]$, which is an easy axis of pure PHO. Here, a pair of antiparallel polarizations are described by antiferroelectric order parameter vector $\mathbf{q} = 1/2(\mathbf{P}_a - \mathbf{P}_b)$, where $\mathbf{P}_a$ and $\mathbf{P}_b$ are polarizations in two adjacent sublattices. Although a pair of antiparallel polarizations along $[101]/[\bar{1}0\bar{1}]$ has zero net polarization, the associated spontaneous elongation of the PHO unit cell along the $[101]$ axis can deform the unit cells of the adjacent BHO and induce a non-zero net polarization in the latter. Specifically, the elongation of PHO cells along $[101]$ leads to both an in-plane expansion (along x or $[100]$) and an out-of-plane expansion (along z or $[001]$). The in-plane expansion of PHO compresses adjacent BHO, leading to the elongation of the latter along z and, hence, the development of non-zero net polarization P_z in BHO. The out-of-plane expansion of PHO also contributes to the elongation of the BHO cells along z and, therefore, the development of P_z. Note that strain-induced P_z in BHO does not produce extra depolarizing field energy because of polarization charge screening from the SRO bottom electrode and the Pt top electrode.

Because the stress imposed by the adjacent PHO relaxes from the PHO/BHO interface toward the center of BHO, the spatial distribution and magnitude of the strain (and, therefore, for the strain-induced polarization) in BHO depend upon its lateral size. As shown in panels b and c of Figure 6 (corresponding to 12 and 2 nm wide BHO, respectively, in Figure 6a), antiparallel polarization pairs of the same magnitude ($|\mathbf{q}|$) are stabilized in antiferroelectric PHO, which is associated with a tensile out-of-plane strain component ε_{zz}. ε_{zz} decreases near the PHO/BHO interface in the PHO region because of the mechanical clamping by BHO. In 12 nm wide BHO, ε_{zz} is larger near the PHO/BHO interface as a result of stress relaxation. The magnitude of strain-induced out-of-plane polarization P_z shows a similar trend in the BHO region, as shown in the top panel of Figure 6b. In comparison, both ε_{zz} and P_z are more uniform in the case of 2 nm wide BHO, as shown in Figure 6c. Moreover, average ε_{zz} and P_z in 2 nm wide BHO are larger than those in 12 nm wide BHO. The asymmetric profiles of ε_{zz} and P_z in the BHO region are caused by the shear strain ε_{xz} transferred from PHO. Such a shear strain also stabilizes a small triangular antiferroelectric domain at the left PHO/BHO interface, with q aligning closer to $[001]/[00\bar{1}]$.

After elucidation of the mechanism for the emergence of ferroelectricity in PBHO solid solution thin films, we further simulated the $P-E$ loops of pure PHO, P7B3HO solid solution, and pure BHO thin films, as shown in panels d, e, and f of Figure 6, respectively. The electric field (E) is applied along the z axis and linearly varied from positive to negative maximum within the same range. In the P7B3HO heterostructure, the 30% BHO regions are placed randomly in the system with three-dimensional (3D) inhomogeneity, as seen in the inset of Figure 6e. The average size of the BHO regions is chosen to be $2 \times 2 \times 2$ nm based on the above discussion, which is consistent with the nanoscale compositional/structural heterogeneity in a solid solution. As shown in Figure 6d, the $P-E$ loop of the pure PHO thin film shows the typical features of double hysteresis for antiferroelectrics. The $P-E$ loop of the pure BHO thin film shown in Figure 6f does not show any hysteresis, as expected for paraelectric materials. However, in the $P-E$ loop of P7B3HO (Figure 6e), an appreciable remnant polarization (larger than that in pure PHO) appears and there is only a single hysteresis loop without a plateau at low-E fields, indicating the emergence of ferroelectricity. Similar to the quasi-1D cases in panels a–c of Figure 6, non-zero net polarization in the present P7B3HO film only emerges from the BHO phase at electrical remanence ($E = 0$). Under an applied electric field, the average out-of-plane polarization $\langle P_z \rangle$ is contributed by both the field-induced growth of out-of-plane polarization in BHO and the development of non-zero net polarization in PHO as a result of the lifted symmetry between two sublattices. Furthermore, in comparison of the three simulated $P-E$ loops (panels d–f of Figure 6), it can be seen that the maximum $\langle P_z \rangle$ is the largest (smallest) in pure PHO (BHO), which is consistent with experiments (c.f., Figure 1c).

CONCLUSION

In conclusion, the solid solution of paraelectric BHO and antiferroelectric PHO had been demonstrated on the STO (001) substrate epitaxially with a compositional spread. The composition-dependent ferroelectric behavior was investigated to reveal the paraelectric–relaxor ferroelectric–ferroelectric–antiferroelectric transition from the composition of 100% BHO to 100% PHO. Moreover, relaxor ferroelectric $Pb_{0.5}Ba_{0.5}HfO_3$ and ferroelectric $Pb_{0.7}Ba_{0.3}HfO_3$ heterostructures were selected as model systems for detailed research. The P5B5HO heterostructure exhibited a typical relaxor ferroelectric behavior with dielectric tunability and great energy storage abilities. In comparison to P5B5HO, P7B3HO behaved more similarly to normal ferroelectricity. Furthermore, the structural origin of ferroelectric properties in P5B5HO and P7B3HO was carefully explored. In addition, the phase field modeling was performed to understand the origin of the ferroelectric feature in PBHO solid solution based on the interaction of the BHO paraelectric state and the PHO antiferroelectric state. A lot of effort was made to look for the critical evidence via STEM. Unfortunately, no microscopic evidence to support the theoretical model has yet been found. We believe the difficulty of identifying antiferroelectric states under STEM is due to the need of a perfect match between the domain size and zone axis. Overall, this study demonstrates the combination of paraelectric and antiferroelectric materials and builds a comprehensive knowledge of the PBHO system for future research and applications in the form of thin films and bulk ceramics.

METHODS

The PBHO and SRO films were deposited on a commercial STO (001) substrate via pulsed laser deposition. Commercial $SrRuO_3$, $BaHfO_3$, $PbHfO_3$, $Pb_{0.5}Ba_{0.5}HfO_3$, and $Pb_{0.7}Ba_{0.3}HfO_3$ targets were adopted in this study. A KrF excimer laser was operated with the laser fluence of 3 J cm^{-2} and laser repetition of 20 Hz. The chamber was first evacuated to a base pressure of 10^{-6} Torr. The deposition of bottom electrode SRO was performed at a substrate temperature of 680 °C in 100 mTorr oxygen pressure. BHO, PHO, and PBHO thin films were deposited at a substrate temperature of 600 °C in 120 mTorr oxygen pressure. For the compositional spread sample, a calibration of growth rate of BHO and PHO was carried out to know how many pulses of laser are needed to accomplish one layer of BHO and PHO. Then, a program-controlled dual-target process was adopted to fabricate the compositional spread samples by controlling the laser pulses of each target with the help of a shadow mask. With the movement of the shadow mask, the composition at different locations can be controlled. After the deposition process, the

https://doi.org/10.1021/acsami.2c02281
ACS Appl. Mater. Interfaces 2022, 14, 22278–22286

heterostructures were cooled with a 0.1 °C s^{-1} cooling rate in 300 Torr oxygen pressure.

The θ–2θ scan, Φ scan, and rocking curve measurements were executed in a Bruker D8 high-resolution X-ray diffractometer with a monochromatic Cu Kα_1 radiation source. RSM was obtained by another X-ray diffractometer (XRD, Smartlab, Rigaku) with Cu Kα_1 radiation. Cross-sectional TEM and STEM were applied to study the microstructure and distribution of elements in the heterostructures by an aberration-corrected scanning transmission electron microscope (JEM-ARM300F, JEOL, Japan) operated at 300 kV and equipped with an X-ray energy-dispersive spectrometer (JED-2300T). A focused ion beam (FIB) system (Helios G4UX, FEI, Hillsboro, OR, U.S.A.) was used to prepare the TEM specimens. The identification of elements and ions was carried out by XPS in ULVAC-PHI PHI 5000 Versaprobe II.

The ferroelectric properties and relative dielectric constant of the PBHO heterostructures were analyzed by the semiconductor analyzer (B1500A, Agilent Technologies). The piezoelectric properties were investigated by PFM (Asylum Research MPF-3D).

In this work, we develop the first phase field model for simulating an equilibrium polarization distribution and its electric-field-induced evolution in a thin-film solid solution of antiferroelectric and paraelectric phases. The model was developed on the basis of existing phase field models for ferroelectric-to-antiferroelectric phase transitions in solid solution bulk material (e.g., $Bi_{1-x}Sm_xFeO_3$[37] and $PbZrO_3$-based ceramic[38]) and ferroelectric-based solid solution relaxor thin films (e.g., $BiFeO_3$–$BaTiO_3$–$SrTiO_3$[39] and $Bi_{0.9}Sm_{0.1}FeO_3$–$SrTiO_3$[40]), respectively. The presence of top and bottom electrodes, the mechanical boundary condition for thin films, and the elastic properties of the $SrTiO_3$ (001) substrate are all considered. Details of our phase field model are shown in the Supporting Information.

■ ASSOCIATED CONTENT

Supporting Information

The Supporting Information is available free of charge at https://pubs.acs.org/doi/10.1021/acsami.2c02281.

XRD measurement, *P*–*E* loops of PBHO, HRTEM, EDS analysis, and information on the phase field model (PDF)

■ AUTHOR INFORMATION

Corresponding Authors

Jia-Mian Hu – *Department of Materials Science and Engineering, University of Wisconsin—Madison, Madison, Wisconsin 53706, United States;* orcid.org/0000-0002-7579-6440; Email: jhu238@wisc.edu

Rong Huang – *Key Laboratory of Polar Materials and Devices, Department of Optoelectronics, East China Normal University, Shanghai 200241, People's Republic of China*; Email: rhuang@ee.ecnu.edu.cn

Ying-Hao Chu – *Department of Materials Science and Engineering, National Yang Ming Chiao Tung University, Hsinchu 30010, Taiwan; Department of Materials Science and Engineering, National Tsing Hua University, Hsinchu 30013, Taiwan;* orcid.org/0000-0002-3435-9084; Email: yhchu@mx.nthu.edu.tw

Authors

Chun-Hao Ma – *Department of Materials Science and Engineering, National Yang Ming Chiao Tung University, Hsinchu 30010, Taiwan*

Yi-Kai Liao – *Department of Materials Science and Engineering, National Yang Ming Chiao Tung University, Hsinchu 30010, Taiwan*

Yunzhe Zheng – *Key Laboratory of Polar Materials and Devices, Department of Optoelectronics, East China Normal University, Shanghai 200241, People's Republic of China*

Shihao Zhuang – *Department of Materials Science and Engineering, University of Wisconsin—Madison, Madison, Wisconsin 53706, United States*

Si-Cheng Lu – *State Key Laboratory of Low Dimensional Quantum Physics and Department of Physics, Tsinghua University, Beijing 100084, People's Republic of China*

Pao-Wen Shao – *Department of Materials Science and Engineering, National Yang Ming Chiao Tung University, Hsinchu 30010, Taiwan*

Jia-Wei Chen – *Department of Materials Science and Engineering, National Yang Ming Chiao Tung University, Hsinchu 30010, Taiwan*

Yu-Hong Lai – *Department of Materials Science and Engineering, National Yang Ming Chiao Tung University, Hsinchu 30010, Taiwan*

Pu Yu – *State Key Laboratory of Low Dimensional Quantum Physics and Department of Physics, Tsinghua University, Beijing 100084, People's Republic of China*

Complete contact information is available at: https://pubs.acs.org/10.1021/acsami.2c02281

Notes

The authors declare no competing financial interest.

■ ACKNOWLEDGMENTS

This work was supported by the National Key Research and Development Program of China (2017YFA0303403), the Ministry of Science and Technology, Taiwan (Grants MOST 109-2124-M-009-009-, 109-2124-M-009-001-MY3, 109-2634-F-009-028, and 110-2224-E-007-002), Academia Sinica, Taiwan (iMATE-107-11), and the Center for Emergent Functional Matter Science of National Yang Ming Chiao Tung University from the Featured Areas Research Center Program within the framework of the Higher Education Sprout Project by the Ministry of Education (MOE) in Taiwan. The work at the University of Wisconsin—Madison was supported by the National Science Foundation (NSF) under the Award CBET-2006028. The phase field simulations were performed using Bridges at the Pittsburgh Supercomputing Center through Allocation TG-DMR180076, which is part of the Extreme Science and Engineering Discovery Environment (XSEDE) and supported by NSF Grant ACI-1548562. The work was also supported by the National Natural Science Foundation of China (Grants 51872155, 52025024, and 61974042).

■ REFERENCES

(1) Cowley, R. A.; Gvasaliya, S. N.; Lushnikov, S. G.; Roessli, B.; Rotaru, G. M. Relaxing with Relaxors: A Review of Relaxor Ferroelectrics. *Adv. Phys.* **2011**, *60* (2), 229–327.

(2) Pandya, S.; Wilbur, J.; Kim, J.; Gao, R.; Dasgupta, A.; Dames, C.; Martin, L. W. Pyroelectric Energy Conversion with Large Energy and Power Density in Relaxor Ferroelectric Thin Films. *Nat. Mater.* **2018**, *17*, 432–438.

(3) Ahn, C. W.; Hong, C.-H.; Choi, B.-Y.; Kim, H.-P.; Han, H.-S.; Hwang, Y.; Jo, W.; Wang, K.; Li, J.-F.; Lee, J.-S.; Kim, I. W. A Brief Review on Relaxor Ferroelectrics and Selected Issues in Lead-Free Relaxors. *J. Korean Phys. Soc.* **2016**, *68*, 1481–1494.

(4) Dawber, M.; Rabe, K. M.; Scott, J. F. Physics of Thin-Film Ferroelectric Oxides. *Rev. Mod. Phys.* **2005**, *77*, 1083.

(5) Liu, Z.; Lu, T.; Ye, J.; Wang, G.; Dong, X.; Withers, R.; Liu, Y. Antiferroelectrics for Energy Storage Applications: A Review. *Adv. Mater. Technol.* **2018**, *3* (9), 1800111.
(6) Zhao, P.; Wang, H.; Wu, L.; Chen, L.; Cai, Z.; Li, L.; Wang, X. High-Performance Relaxor Ferroelectric Materials for Energy Storage Applications. *Adv. Energy Mater.* **2019**, *9* (17), 1803048.
(7) Martin, L. W.; Rappe, A. M. Thin-Film Ferroelectric Materials and Their Applications. *Nat. Rev. Mater.* **2017**, *2*, 16087.
(8) Zhou, Z.; Yang, Q.; Liu, M.; Zhang, Z.; Zhang, X.; Sun, D.; Nan, T.; Sun, N.; Chen, X. Antiferroelectric Materials, Applications and Recent Progress on Multiferroic Heterostructures. *Spin* **2015**, *5* (1), 1530001.
(9) Lin, Y.; Li, D.; Zhang, M.; Zhan, S.; Yang, Y.; Yang, H.; Yuan, Q. Excellent Energy-Storage Properties Achieved in $BaTiO_3$-Based Lead-Free Relaxor Ferroelectric Ceramics via Domain Engineering on the Nanoscale. *ACS Appl. Mater. Interfaces* **2019**, *11*, 36824−36830.
(10) Li, F.; Zhang, S.; Yang, T.; Xu, Z.; Zhang, N.; Liu, G.; Wang, J.; Wang, J.; Cheng, Z.; Ye, Z.-G.; Luo, J.; Shrout, T. R.; Chen, L.-Q. The Origin of Ultrahigh Piezoelectricity in Relaxor-Ferroelectric Solid Solution Crystals. *Nat. Commun.* **2016**, *7* (1), 13807.
(11) Zhang, L.-L.; Huang, Y.-N. Theory of Relaxor-Ferroelectricity. *Sci. Rep.* **2020**, *10* (1), 5060.
(12) Kamba, S.; Kempa, M.; Bovtun, V.; Petzelt, J.; Brinkman, K.; Setter, N. Soft and Central Mode Behaviour in $PbMg_{1/3}Nb_{2/3}O_3$ Relaxor Ferroelectric. *J. Phys.: Condens. Matter* **2005**, *17*, 3965.
(13) Zhang, S.; Li, F. High Performance Ferroelectric Relaxor-$PbTiO_3$ Single Crystals: Status and Perspective. *J. Appl. Phys.* **2012**, *111*, 031301.
(14) Zhang, S.; Li, F.; Jiang, X.; Kim, J.; Luo, J.; Geng, X. Advantages and Challenges of Relaxor-$PbTiO_3$ Ferroelectric Crystals for Electroacoustic Transducers − A Review. *Prog. Mater. Sci.* **2015**, *68*, 1−66.
(15) Li, F.; Cabral, M. J.; Xu, B.; Cheng, Z.; Dickey, E. C.; LeBeau, J. M.; Wang, J.; Luo, J.; Taylor, S.; Hackenberger, W.; Bellaiche, L.; Xu, Z.; Chen, L.-Q.; Shrout, T. R.; Zhang, S. Giant Piezoelectricity of Sm-Doped $Pb(Mg_{1/3}Nb_{2/3})O_3$-$PbTiO_3$ Single Crystals. *Science* **2019**, *364* (6437), 264−268.
(16) Ye, Z.-G. High-Performance Piezoelectric Single Crystals of Complex Perovskite Solid Solutions. *MRS Bull.* **2009**, *34* (4), 277−283.
(17) Baek, S.-H.; Rzchowski, M. S.; Aksyuk, V. A. Giant Piezoelectricity in PMN-PT Thin Films: Beyond PZT. *MRS Bull.* **2012**, *37* (11), 1022−1029.
(18) Hao, X.; Zhai, J.; Kong, L. B.; Xu, Z. A Comprehensive Review on the Progress of Lead Zirconate-Based Antiferroelectric Materials. *Prog. Mater. Sci.* **2014**, *63*, 1−57.
(19) Mani, B. K.; Lisenkov, S.; Ponomareva, I. Finite-Temperature Properties of Antiferroelectric $PbZrO_3$ from Atomistic Simulations. *Phys. Rev. B* **2015**, *91*, 134112.
(20) Izyumskaya, N.; Alivov, Y.-I.; Cho, S.-J.; Morkoç, H.; Lee, H.; Kang, Y.-S. Processing, Structure, Properties, and Applications of PZT Thin Films. *Crit. Rev. Solid State Mater. Sci.* **2007**, *32* (3−4), 111−202.
(21) Choi, K. J.; Biegalski, M.; Li, Y. L.; Sharan, A.; Schubert, J.; Uecker, R.; Reiche, P.; Chen, Y. B.; Pan, X. Q.; Gopalan, V.; Chen, L.-Q.; Schlom, D. G.; Eom, C. B. Enhancement of Ferroelectricity in Strained $BaTiO_3$ Thin Films. *Science* **2004**, *306* (5698), 1005−1009.
(22) Acosta, M.; Novak, N.; Rojas, V.; Patel, S.; Vaish, R.; Koruza, J.; Rossetti, G. A., Jr.; Rödel, J. $BaTiO_3$-Based Piezoelectrics: Fundamentals, Current Status, and Perspectives. *Appl. Phys. Rev.* **2017**, *4*, 041305.
(23) Lei, C.; Bokov, A. A.; Ye, Z.-G. Ferroelectric to Relaxor Crossover and Dielectric Phase Diagram in the $BaTiO_3$-$BaSnO_3$ System. *J. Appl. Phys.* **2007**, *101*, 084105.
(24) Wang, D.; Bokov, A. A.; Ye, Z.-G.; Hlinka, J.; Bellaiche, L. Subterahertz Delectric Relaxation in Lead-Free $Ba(Zr,Ti)O_3$ Relaxor Ferroelectrics. *Nat. Commun.* **2016**, *7* (1), 11014.
(25) Prosandeev, S.; Wang, D.; Bellaiche, L. Properties of Epitaxial Films Made of Relaxor Ferroelectrics. *Phys. Rev. Lett.* **2013**, *111* (24), 247602.
(26) Akbarzadeh, A. R.; Prosandeev, S.; Walter, E. J.; Al-Barakaty, A.; Bellaiche, L. Finite-Temperature Properties of $Ba(Zr, Ti)O_3$ Relaxors from First Principles. *Phys. Rev. Lett.* **2012**, *108* (25), 257601.
(27) Acharya, M.; Banyas, E.; Ramesh, M.; Jiang, Y.; Fernandez, A.; Dasgupta, A.; Ling, H.; Hanrahan, B.; Persson, K.; Neaton, J. B.; Martin, L. W. Exploring the $Pb_{1-x}Sr_xHfO_3$ System and Potential for High Capacitive Energy Storage Density and Efficiency. *Adv. Mater.* **2022**, *34*, 2105967.
(28) Garten, L. M.; Dwaraknath, S.; Walker, J.; Mangum, J. S.; Ndione, P. F.; Park, Y.; Beaton, D. A.; Gopalan, V.; Gorman, B. P.; Schelhas, L. T.; Toney, M. F.; Trolier-McKinstry, S.; Persson, K. A.; Ginley, D. S. Theory-Guided Synthesis of a Metastable Lead-Free Piezoelectric Polymorph. *Adv. Mater.* **2018**, *30*, 1800559.
(29) Wei, J.; Yang, T.; Wang, H. Excellent Energy Storage and Charge-Discharge Performances in $PbHfO_3$ Antiferroelectric Ceramics. *J. Eur. Ceram. Soc.* **2019**, *39*, 624−630.
(30) Huang, X.-X.; Zhang, T.-F.; Gao, R.-Z.; Huang, H.-B.; Ge, P.-Z.; Tang, H.; Tang, X.-G. Large Room Temperature Negative Electrocaloric Effect in Novel Antiferroelectric $PbHfO_3$ Films. *ACS Appl. Mater. Interfaces* **2021**, *13* (18), 21331−21337.
(31) Bouhemadou, A.; Djabi, F.; Khenata, R. First Principles Study of Structural Elastic Electronic and Optical Properties of the Cubic Perovskite $BaHfO_3$. *Phys. Lett. A* **2008**, *372* (24), 4527−4531.
(32) Kim, Y. M.; Park, C.; Ha, T.; Kim, U.; Kim, N.; Shin, J.; Kim, Y.; Yu, J.; Kim, J. H.; Char, K. High-K Perovskite Gate Oxide $BaHfO_3$. *APL Mater.* **2017**, *5*, 016104.
(33) Huang, Y.-L.; Liu, H.-J.; Ma, C.-H.; Yu, P.; Chu, Y.-H.; Yang, J.-C. Pulsed Laser Deposition of Complex Oxide Heteroepitaxy. *Chin. J. Phys.* **2019**, *60*, 481−501.
(34) Kumar, A.; Baker, J. N.; Bowes, P. C.; Cabral, M. J.; Zhang, S.; Dickey, E. C.; Irving, D. L.; LeBeau, J. M. Atomic-Resolution Electron Microscopy of Nanoscale Local Structure in Lead-Based Relaxor Ferroelectrics. *Nat. Mater.* **2021**, *20*, 62−67.
(35) Krogstad, M. J.; Gehring, P. M.; Rosenkranz, S.; Osborn, R.; Ye, F.; Liu, Y.; Ruff, J. P. C.; Chen, W.; Wozniak, J. M.; Luo, H.; Chmaissem, O.; Ye, Z.-G.; Phelan, D. The Relation of Local Order to Material Properties in Relaxor Ferroelectrics. *Nat. Mater.* **2018**, *17*, 718−724.
(36) Enriquez, E.; Li, Q.; Bowlan, P.; Lu, P.; Zhang, B.; Li, L.; Wang, H.; Taylor, A. J.; Yarotski, D.; Prasankumar, R. P.; Kalinin, S. V.; Jia, Q.; Chen, A. Induced Ferroelectric Phases in $SrTiO_3$ by a Nanocomposite Approach. *Nanoscale* **2020**, *12* (35), 18193−18199.
(37) Xue, F.; Liang, L.; Gu, Y.; Takeuchi, I.; Kalinin, S. V.; Chen, L.-Q. Composition- and Pressure-Induced Ferroelectric to Antiferroelectric Phase Transitions in Sm-Doped $BiFeO_3$ System. *Appl. Phys. Lett.* **2015**, *106*, 012903.
(38) Fan, Z.; Xue, F.; Tutuncu, G.; Chen, L.-Q.; Tan, X. Interaction Dynamics Between Ferroelectric and Antiferroelectric Domains in a $PbZrO_3$-Based Ceramic. *Phys. Rev. Appl.* **2019**, *11*, 064050.
(39) Pan, H.; Li, F.; Liu, Y.; Zhang, Q.; Wang, M.; Lan, S.; Zheng, Y.; Ma, J.; Gu, L.; Shen, Y.; Yu, P.; Zhang, S.; Chen, L.-Q.; Lin, Y.-H.; Nan, C.-W. Ultrahigh−Energy Density Lead-Free Dielectric Films via Polymorphic Nanodomain Design. *Science* **2019**, *365*, 578−582.
(40) Pan, H.; Lan, S.; Xu, S.; Zhang, Q.; Yao, H.; Liu, Y.; Meng, F.; Guo, E.-J.; Gu, L.; Yi, D.; Wang, X. R.; Huang, H.; MacManus-Driscoll, J. L.; Chen, L.-Q.; Jin, K.-J.; Nan, C.-W.; Lin, Y.-H. Ultrahigh Energy Storage in Superparaelectric Relaxor Ferroelectrics. *Science* **2021**, *374* (6563), 100−104.
(41) Li, F.; Lin, D.; Chen, Z.; Cheng, Z.; Wang, J.; Li, C.; Xu, Z.; Huang, Q.; Liao, X.; Chen, L.-Q.; Shrout, T. R.; Zhang, S. Ultrahigh Piezoelectricity in Ferroelectric Ceramics by Design. *Nat. Mater.* **2018**, *17*, 349−354.